A Reference-Free Debonding Monitoring Technique in CFRP Strengthened RC Structures Using Active Sensing Materials

Seung Dae Kim[1], Chi Won In[2], Kelly E. Cornin[3]
([1]*Ph.D. Candidate,* [2]*Master Student,* [3]*Undergraduate Student, Carnegie Mellon University, Pittsburgh, PA, USA*)

ABSTRACT

This study proposes a new concept of real-time nondestructive testing (NDT) for debonding monitoring, which continuously inspects the bonding condition between carbon fiber-reinforced polymer (CFRP) and host reinforced concrete (RC) structures. The uniqueness of this new NDT concept is in detecting debonding *without relying on previously-obtained baseline data*. The proposed reference-free damage diagnosis is achieved based on the concept of time reversal acoustics (TRA). According to TRA, an input signal at an excitation point can be reconstructed if the response signal measured at another point is reemitted to the original excitation point after being reversed in the time domain. A nonlinear damage along the wave propagation path generates the deviation of the reconstructed signal from the known initial input signal. This discrepancy of the two signals allows instantaneous identification of damage without requiring a baseline signal representing the undamaged state for comparison. The concept of TRA has been extended to guided-wave propagation within the CFRP-strengthened RC beams to improve the detectability of local debonding. Monotonic and fatigue load tests of large-scale CFRP-strengthened RC beams are conducted to demonstrate the potential of the proposed reference-free debonding monitoring system.

Keywords: active sensing, baseline-free nondestructive testing, carbon fiber reinforced polymer, debonding, structural health monitoring, time-reversal acoustics.

1. INTRODUCTION

Carbon fiber reinforced polymer (CFRP) composite materials have become an attractive alternate material for retrofit and rehabilitation of structural members of bridges such as beams and slabs due to their outstanding strength, light weight and versatility (Karbhari et al. 2000). However, the improvement of strength and stiffness in a host structure can only be guaranteed when a reliable bonding condition between the host member and the added CFRP materials is maintained. Therefore, a reliable nondestructive testing (NDT) system is required to monitor the initial installation quality and the long-term efficiency of bonding. There has been a large volume of research on debonding detection for FRP strengthened concrete structures. Infrared thermograph (Levar and Hamilton 2003), fiber optic sensing (Ansari 2005), electromechanical impedance spectrum (Giurgiutiu et al. 2003), electrochemical impedance spectroscopy methods (Hong and Harichandran 2005), and microwave sensing (Akuthota et al. 2004, Ekenel et al. 2004, Feng et al. 2000a) have been previously applied. These techniques are shown to successfully identify FRP debonding. However, data interpretation often needs to be manually performed by experienced engineers, and automation of data analysis remains largely unsolved. For continuous monitoring, it will be critical to reduce unnecessary interference by users and to automate the data analysis process as much as possible. In addition, although many damage detection techniques are successfully applied to scaled models or specimens tested in controlled laboratory environments, the performance of these techniques in real operational environments is still questionable and needs to be validated. Varying environmental and operational conditions produce changes in the dynamic response of bridge system that can be easily mistaken for damage (Sohn 2006). It is challenging to develop a NDT technique with minimal false positive and negative indications of damage in these conditions. Few NDT systems have been developed with the intent of deploying it for continuous monitoring of in-service structures.

The ultimate goal of this study is to develop a continuous NDT technique that goes beyond the laboratory demonstration and can be deployed in real bridge structures. To achieve this goal, a new NDT technique is developed by applying the concept of time reversal acoustics (TRA) (Fink and Prada 2001) to guided wave propagations (Rose 1999 and Viktorov 1967) within CFRP-strengthened RC beams. Based on TRA, an input signal at an excitation point can be reconstructed if the response signal measured at another point is reemitted to the original excitation point after being reversed in the time domain. This time reversibility is based on linear reciprocity of elastic waves, and breaks down when there is a source of nonlinearity along the wave propagation path. Because certain types of defects introduce nonlinear responses, examining the deviation of the reconstructed signal from the known initial input signal allows instantaneous identification of damage without requiring a direct comparison with previously-obtained baseline signal data. This novel concept is extended to develop a NDT system that can be rapidly deployed on laboratory specimens or in-field structures and autonomously perform local damage diagnoses at the presence of operational and environmental variation that in-service structures encounter. Smart

materials such as lead zirconate titanate (PZT) are used for both generating and measuring guided waves (Giurgiutiu and Lyshevski 2004).

2. THEORETICAL BACKGROUND FOR WAVE PROPAGATION IN SOLID CONTINUA

In this study, elastic waves propagating in solid continua are used for debonding detection. These elastic waves can be classified into body and guided waves, which are governed by the Navier's partial differential equations (Rose 1999 and Viktorov 1967). While body waves are not constrained by any boundaries, guided waves need to satisfy the boundary conditions imposed by the physical systems as well as the governing equations. Guided waves can be further divided into Lamb, Stoneley and Rayleigh surface waves depending on the boundary conditions.

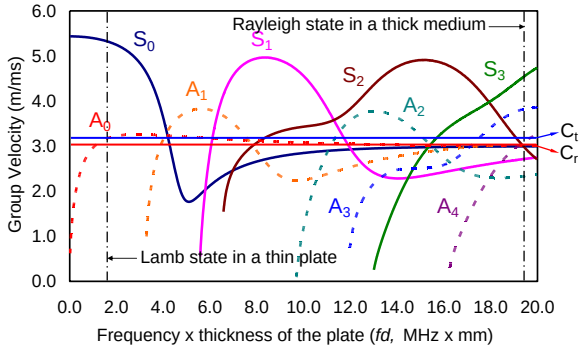

(a) A typical dispersion curve of Lamb wave in a thin plate

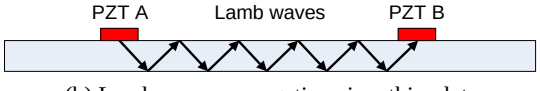

(b) Lamb wave propagations in a thin plate

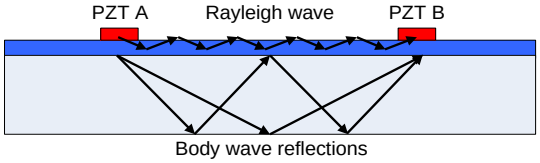

(c) Complex guided wave propagations in a layered medium with two distinctively different thicknesses

Figure 1: Comparison of wave propagation characteristics between a thin plate and a layered medium with two distinctively different thicknesses

Among these three types of guided waves, Lamb waves exist in thin plate-like structures; they are strain waves constrained by two closely-spaced free surfaces (Viktorov 1967). The analysis and interpretation of Lamb waves can be complicated due to their dispersive and multimodal natures as shown in Figure 1(a). Due to dispersion characteristics, the various frequency components of symmetric and anti-symmetric Lamb waves travel at different speeds and attenuate at different rates, causing the shapes of wave packets to change as they propagate through a solid continuum. In spite of its unique dispersion and multimode characteristics, Lamb waves are widely used for defect detection in aerospace structures due to their relatively long sensing range (Ing and Fink 1996, Kessler et al. 2003, Mal et al. 2005 and Sohn et al. 2005). Because Lamb wave propagations are well guided within two closely spaced boundaries as shown in Figure 1(b), the Lamb waves can travel a long distance with little attenuation. As the thickness of the plate (or the product of the exciting frequency (f) and the thickness of the plate (d) in Figure 1) increases, the fundamental symmetric (S_0) and anti-symmetric (A_0) Lamb modes converge to a Rayleigh surface wave (C_r), higher modes merge to a transverse bulk wave (C_t), and additional body waves appear as shown in Figure 1(c). Wave propagation characteristics are further complicated when a thin layer is attached to a thick medium. An RC beam with a CFRP layer is a good example of such a layered structure with two distinctively different thicknesses. Luangvilai et al. (2002) experimentally obtained the dispersion curve of a concrete beam with a CFRP layer and demonstrated the complexity of its wave propagation characteristics. Therefore, a conventional Lamb wave approach may not be applicable for the monitoring of CFRP-RC beam coupled structures, and a new approach, which can be used regardless of the complexity of waves, is necessary. To address this issue, the concept of TRA is applied to guided wave propagations.

3. TIME REVERSAL ACOUSTICS

The origin of the proposed time reversal process traces back to TRA (Fink and Prada 2001). An example of TRA can be found in everyday life: If one screams "Hello" at the summit of a mountain toward another mountain, the sound will hit the second mountain and bounce back. One hears "Hello" as an echo. This time reversibility of acoustic (or body) waves has found applications in lithotripsy, ultrasonic brain surgery, nondestructive evaluation, and acoustic communications (Fink 1999). However, the time reversibility does not work well in guided waves due to their multimode and dispersion characteristics. A combination of a specific narrowband input waveform and multi-resolution signal processing is employed so that the time reversibility of guided waves is preserved within an acceptable tolerance for more complex configurations such as the layered structure presented in this study (Park et al. 2004).

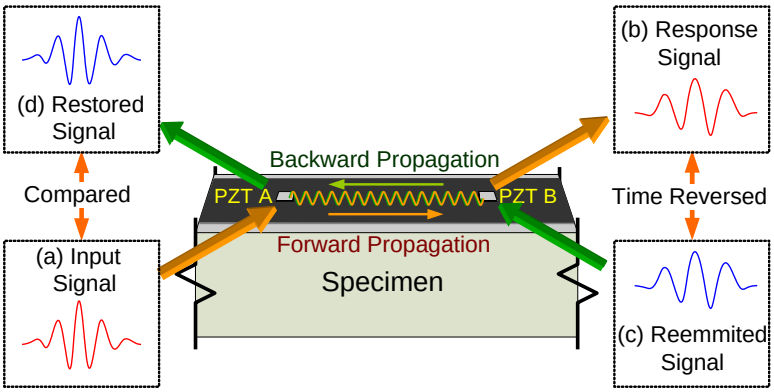

Figure 2: Schematic concept of TRA-based damage identification that does not require any pas baseline signals: (a) a known input signal is applied to PZT A, (b) the corresponding response is measured at PZT B, (c) the response at PZT B is reversed in the time domain and applied back to PZT B, and (d) the final response is measured at PZT A. The shape of this reconstructed signal should be identical to the original input signal without defect along the wave propagation path.

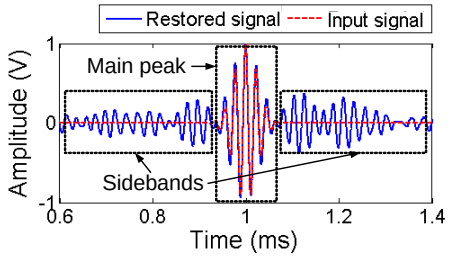

Figure 3: The creation of multiple sidebands in a reconstructed signal due to multimodes, multiple wave propagation paths, and reflective waves

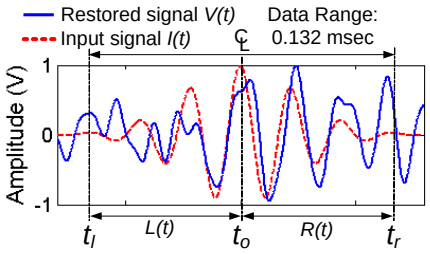

Figure 4: Definition of t_l, t_o, and t_r used in Equation (1) & (2)

In the extended time reversal process, a narrowband input signal can be reconstructed at an excitation point (PZT A) if an output signal recorded at another point (PZT B) is reemitted to the original source point (PZT A) after being reversed and scaled in the time domain as shown in Figure 2. This process is referred to as the time reversibility of waves and is based on the spatial reciprocity and time-reversal invariance of linear wave equations (Draeger et al. 1997). However, due to the existence of multiple wave modes, wave propagation paths and reflections, the actually reconstructed signal has several "sidebands" as shown in Figure 3. It is noted that the shape of the "main peak", where most of energy converges, remains identical to the original input signal, although the amplitude of the reconstructed signal is smaller than that of the original input signal due to attenuation. In Figure 3 and Figure 4, the reconstructed signal is scaled so that the shape of the main peak in the reconstructed signal can be better compared with that of the input signal.

Damage detection using the time reversal process is based on the premise that if there are certain types of defect along the wave propagation path, time reversibility breaks down. More precisely, the shape of the reconstructed signal's main peak will depart from that of the original input signal. By examining the deviation of the restored signal's main peak from the known input signal as shown in Figure 4, certain types of damage can be identified without requiring any previously obtained baseline signals. Based on this premise, two indices are proposed for damage identification: time reversibility (TR) and symmetry (SYM) indices. The TR index, defined below, compares the waveform of the original input with that of the reconstructed signal:

$$\mathrm{TR} = 1 - \sqrt{\left\{\int_{t_l}^{t_r} I(t)V(t)\,dt\right\}^2 \Big/ \left\{\int_{t_l}^{t_r} I(t)^2\,dt \int_{t_l}^{t_r} V(t)^2\,dt\right\}} \qquad (1)$$

where $I(t)$ and $V(t)$ denote the known input signal and the main peak in the reconstructed signal, respectively. For the experimental study presented, a 7-peak toneburst signal is used for excitation; t_l and t_r represent the starting and ending time points of the toneburst signal as defined in Figure 4. The value of the TR index becomes zero when the shape of the main peak in the reconstructed signal is identical to that of the original input signal. Note that the

amplitude scaling difference between *I(t)* and *V(t)* does not affect the TR value. If *V(t)* deviates from *I(t)*, the TR index value increases and approaches 1.0, indicating the existence of damage along the wave propagation path. The SYM index measures the degree of symmetry of the reconstructed signal with respect to the main peak in the middle.

$$\mathrm{SYM} = 1 - \sqrt{\left\{\int_{t_o}^{t_r} L(-t)R(t)dt\right\}^2 \Big/ \left\{\int_{t_l}^{t_o} L(t)^2 dt \int_{t_o}^{t_r} R(t)^2 dt\right\}} \qquad (2)$$

where *L(t)* and *R(t)* denote the left-hand and right-hand sides of the reconstructed signal with respect to the main peak, t_o is the center time point of the main peak, and t_l and t_r represent the starting and ending time points as defined for the TR index. All terms are shown in Figure 4

4. DESCRIPTIONS OF EXPERIMENTS

The overall configuration of the test specimen is shown in Figure 5. The test specimen consists of a RC beam with a surface mounted preformed CFRP strip. The RC beam is 254 mm deep, 152 mm wide and simply supported over 4750 mm as shown in Figure 5. It is reinforced with 3 #4 (13 mm diameter) primary and 2 #3 (9 mm diameter) compression reinforcing bars. The soffit-applied preformed CFRP strip is 102 mm wide and 1.3 mm thick, and the strip has a rupture strength and tensile modulus of 155 MPa and 2.8 MPa, respectively. This CFRP layer is applied over the middle 3750 mm of the beam span using an epoxy-based structural adhesive with a modulus of 2.2 MPa and a rupture strain of 0.006. Two such beam specimens, shown in Figure 5(c), were used in this study. The load and strain data acquisition system (DAQ2 in Figure 5(d)) includes (1) four strain gauges (labeled as 1 to 4 in Figure 5(a)) attached to the reinforcing steel bars, (2) eight additional strain gauges mounted on the surface of the CFRP layer coincident with the previous strain gauges (labeled 5 to 12 in Figure 5(a)), and (3) a load cell and displacement transducer for measuring the applied load and displacement at the midspan of the beam. Note that Figure 5(a) shows the beam in an inverted position. These instruments were used to measure strains and to identify the presence of debonding at the discrete gauge locations. Details of the experimental setup and data analysis results based on strain measurements can be found in Reeve (2005) and Zorn (2006).

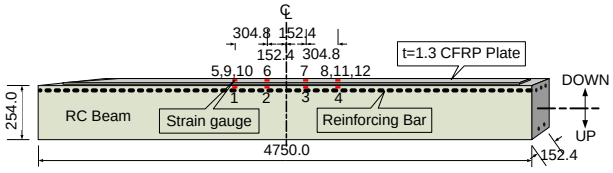

(a) Elevation of a CFRP strengthened RC beam with strain gauge locations (shown upside down)

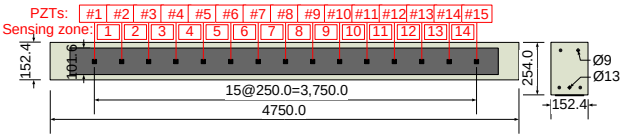

(b) An inverted plan view of the CFRP strengthened RC beam showing the PZT sensors and the sensing zones

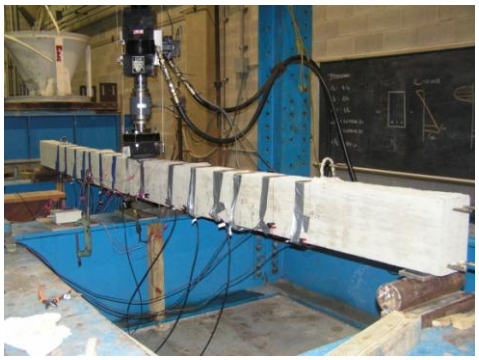

(c) Testing configuration

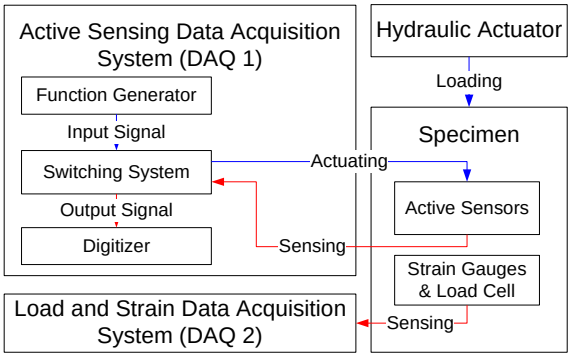

(d) A layout of the active sensing data acquisition

Figure 5: Test setup and configuration of strain gauge and active sensing devices embedded/attached to the CFRP strengthened RC beam (all units are in mm)

A total of 15 square PZT wafers (2 cm x 2 cm x 0.0508 cm) were attached on the free surface of the CFRP layer to form a distributed active sensing system (Figure 5(b)). Because the PZTs produce an electrical charge when deformed, the PZT wafers were used as dynamic strain gauges in DAQ1 shown in Figure 5(d). The same PZT wafers are also used as actuators, because elastic waves are produced when an electrical field is applied to the wafers (Sun et al. 1995). In this experiment, excitation signals were applied to even number PZT wafers, and

responses were measured at odd number PZTs. For instance, a 7-peak toneburst signal was applied to PZT #2, and the corresponding forward signal was measured at PZT #1. Then, the measured forward signal was time-reversed and applied at PZT #2 again, and the reconstructed signal was measured at PZT #1. This time reversal process was repeated for a total of 14 different path combinations (PZTs #2–#1, PZTs #2–#3, … , and PZTs #14–#15). These 14 sensing segments were referred to as sensing zones #1 to #14 in Figure 5(b). The driving frequency value and the sampling rate of the digitizer were set to 45 kHz and 5 MHz, respectively. During the time reversal process, 10,000 time data points, equal to 2 msec, were collected and time-reversed. The length of the time-reversed signal was selected to be long enough so that the majority of the mechanical responses were captured within the time segment.

Three loading cases were investigated in this study (Cases I-III). In Case I (Specimen L4 reported in Reeve 2005), one of the two large-scale specimens was subjected to incremental monotonic loading, and the data from the active sensing system were collected at each loading step. The monotonic load was gradually increased until the specimen failed. The loading was initially force-controlled up to loading step 5 (40.03kN) and then switched to a displacement control as the beam "yielded" starting from loading step 6 (41.59 KN) to loading step 24 (44.54 kN). The second specimen (Specimen L4F reported in Zorn 2006) was first subjected to fatigue loading in Case II and subsequently to monotonic loading to failure in Case III. In Case II, cyclic loads with a driving frequency of 1.3Hz and an applied load range of 4.45 kN to 22.24 kN were applied. The specimen underwent a total of 2,000,000 fatigue load cycles over 16 days. Data from the active sensing system were gathered at several loading cycles: N = 0, 1, 100, 200, 500, 1000, 2000, 5000, 10000, 162330, 308800, 439880, 609490, 721990, 891160, 1030700, 1175690, 1321900, 1428920, 1564430, 1651580, 1786920, 1896400, 2000000 cycles. During the data collection from the active sensing system, the cyclic load was paused at the minimum load of 4.45 kN. A monotonic load test similar to Case I was performed on the second specimen following the fatigue-conditioning described above. This was referred to as Case III. Data were measured at 14 loading steps (13.34kN to 48.11kN). The force controlled loading was initially applied up to loading step 4 (36.90kN), and the loading was changed to the displacement control up to loading step 14 (48.11kN). In all three cases, the loading was applied at the mid-point of the simply supported beam, and data from the active sensing devices were collected while the load was held constant.

5. EXPERIMENTAL RESULTS

The monotonic and fatigue load tests were performed on two CFRP strengthened RC beams to introduce debonding between the CFRP layers and the RC beams, and data were periodically collected from the active sensing system during the loading tests. Damage diagnosis based on the measured data is presented in this section for all three loading cases (Cases I-III).

5.1 Case I: Monotonic Loading

The damage diagnosis obtained during the monotonic loading test of the first CFRP-RC beam specimen is presented in Figure 6. In Figure 6, the TR and SYM indices defined in Eqs. (1) and (2) are shown along the length of the beam and computed at selective loading steps (1, 2, 6, 7, 15 and 24). The sensing zones in Figure 6 are defined in Figure 5(b). It is observed from Figure 6 that: (1) At loading step 2, there was a significant increase of the TR and SYM indices at the mid-span point (sensing zone 7); and (2) As loading increased, larger TR and SYM index values were observed near sensing zones 5 and 10. It is speculated that the initial increases of the TR and SYM indices at the mid-span (sensing zone 7) did not result from debonding but rather from initial cracking of the concrete beam. An additional anomaly in sensing zone 7 was a 4.8 mm diameter steel rod embedded in the concrete used to connect the midspan displacement transducer whose presence may have affected the TR and SYM values. Further study is underway to better understand the sources of these abnormal values. In this study, these TR and SYM outlier values not related to debonding were disregarded. Overall, the findings from the proposed system agreed well with visual inspection performed after the completion of the monotonic load test and the data obtained from the strain gauge system (Reeve 2005). Figure 7 shows the debonding regions identified by either a visual inspection or a coin-tapping test after the completion of the test. The largest debonding was observed near sensing zones 5 and 10, which coincide with the results shown in Figure 6.

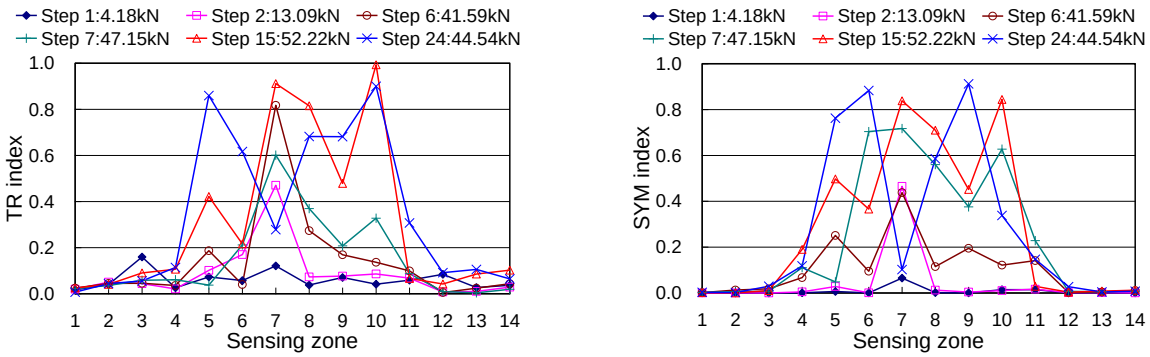

(a) TR indices at 6 selective loading steps (b) SYM indices at 6 selective loading steps

Figure 6: Changes of the TR and SYM indices measured at selective loading steps during the Case I monotonic loading test

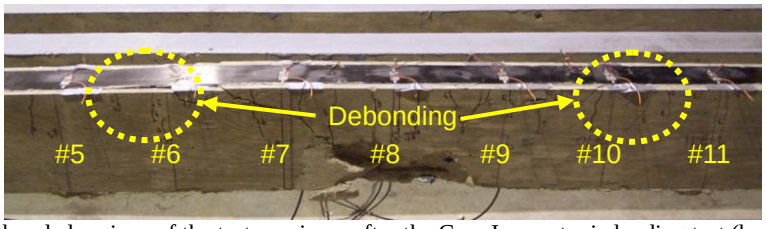

Figure 7: Debonded regions of the test specimen after the Case I monotonic loading test (beam inverted)

Next, the TR and SYM indices values at sensing zones 10 and 14 are plotted as a function of the 24 loading steps in Figure 8: Sensing zone 10 is where the greatest debonding is observed along the beam length, and sensing zone 14 is located at the end of the beam where no debonding is expected. Figure 8 shows that the TR and SYM indices significantly increased at loading step 5 near sensing zone 10, but they did not vary much near sensing zone 14 throughout the entire loading steps. This finding is again in good agreement with the visual inspection performed after the completion of the monotonic loading test. In contrast, the conventional strain gauge instrumentation was only able to capture debonding as the debonding front passed the discrete location of the gauges.

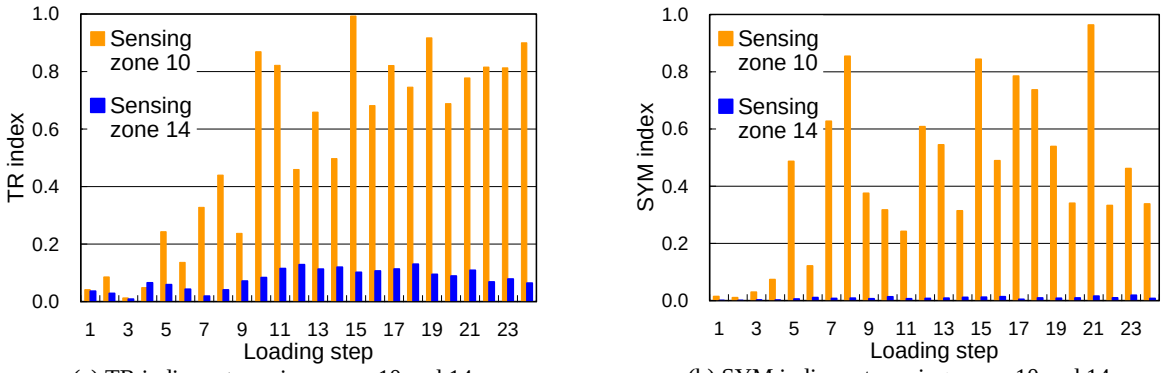

(a) TR indices at sensing zones 10 and 14 (b) SYM indices at sensing zones 10 and 14

Figure 8: Changes of TR and SYM indices as a function of incremental monotonic loading measured at sensing zones 10 and 14 for Case I

The forwarding and reconstructed signals measured at sensing zones 10 and 14 are presented in Figure 9 for selective loading steps (1, 7 and 24). In these figures, the "forwarding" signal is the direct response signal measured at the sensing PZT when the known excitation signal is applied to the exciting PZT. For example, the forwarding signal in Figure 9(a) shows the response signal measured at PZT #11 when the excitation waveform is applied to PZT #10. Then, the measured signal at PZT #11 is time-reversed and applied back to PZT #10. The corresponding response signal is measured at PZT #11; this is the "reconstructed" signal shown in Figure 9(a). The following observations are made from Figure 9: (1) As the load level increased, the static deflection of the beam increased near sensing zone 10. Consequently, the strain of the PZT material exceeded the maximum strain specified by the manufacturer (so-called "strain saturation"), and its response to the elastic waves became less sensitive as shown in

Figure 9(a); (2) Deviation of the reconstructed signal (solid line) from the original input signal (dashed line) was observed at the increased load levels, indicating the initiation of debonding near sensing zone 10. To verify that the increases of the TR and SYM indices were not caused by the large strain deformation of the PZTs, a new set of PZT wafers were attached side-by-side to the existing PZTs #5 through #11 following the completion of the monotonic load test as shown in Figure 10(a). The results from this new set of PZT wafers are summarized in Figure 10(b). The data from the new PZT series was consistent with the post-test observations presented in Figure 10 and with the TR and SYM indices obtained from the original PZTs. Therefore, the changes of the TR and SYM indices are concluded to be related to debonding rather than PZT defects or strain saturation.

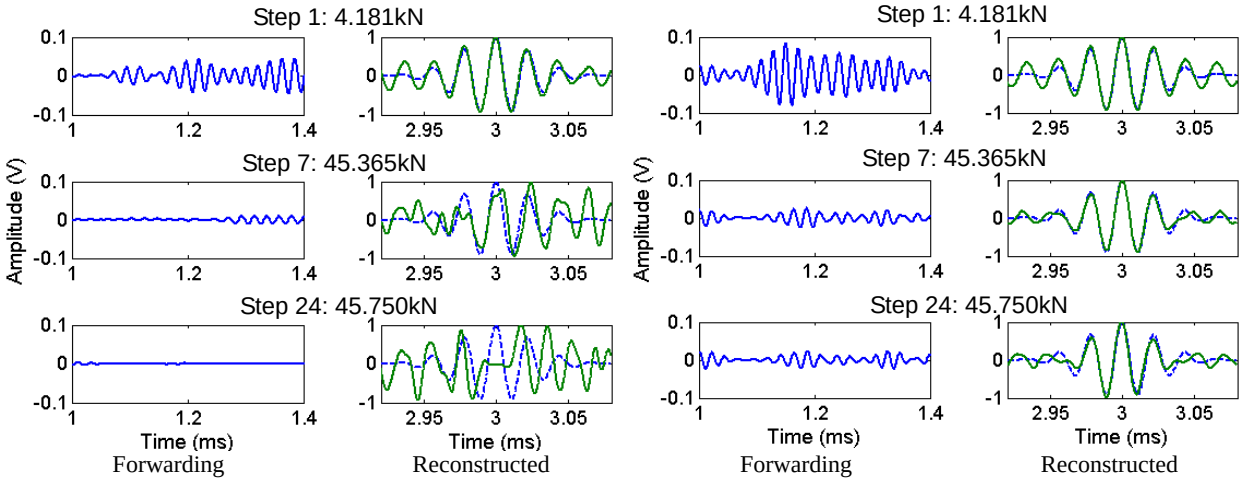

(a) Sensing zone 10 (b) Sensing zone 14

Figure 9: Forwarding and reconstructed signals measured at sensing zones 10 and 14 for Case I

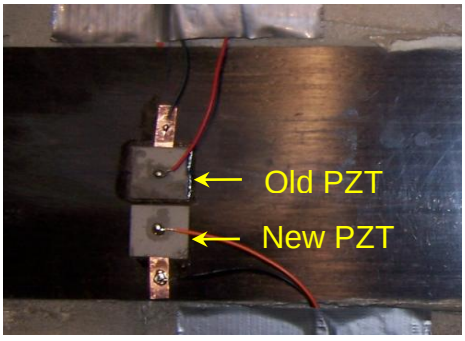

(a) New PZTs attached next to PZTs #5 - #11 for signal verification

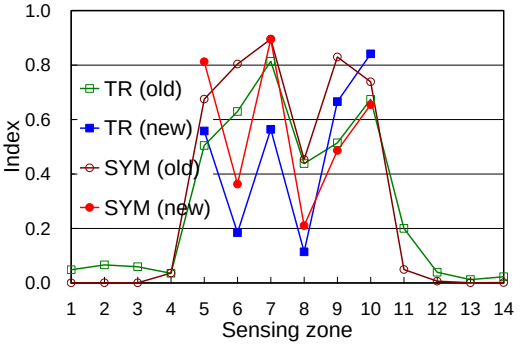

(b) Comparison of TR and SYM indices obtained from the old and new PZTs

Figure 10: Examination of PZT sensor functionality: New set of PZTs are attached side-by-side to PZTs #5 - #11 to inspect the proper performance of the PZT sensors after the Case I monotonic loading test

Qualitatively different results were obtained from sensing zone 14 located near one end of the beam. As mentioned previously, no sign of debonding was expected or found near sensing zone 14. This is consistent with the finding that the reconstructed signal in Figure 9(b) did not change much throughout the entire loading history. However, it should be noted that the forwarding signal continuously changed as loading progressed. This observation clearly demonstrates the advantage of adopting the reconstructed signal for damage diagnosis rather than the conventional method of using only the forwarding signal: While the forwarding signal is sensitive to normal operational variations of the system that are not necessarily related to defects (increased beam shear force, in this case), the reconstructed signal seems to be more robust against these normal variations. Therefore, it is expected that the proposed debonding monitoring system based on the time reversal concept is more suitable for bridge field deployment and efficient for minimizing false-positive indications of defects.

5.2 Case II: Fatigue Cyclic Loading Test

The second specimen was subjected to 2,000,000 cycles of fatigue loading. As shown in Figure 11, there was no sign of CFRP strip debonding from the substrate concrete beam during the fatigue loading test nor was any evidence of debonding found from visual inspection or a coin tapping test performed following the fatigue loading test. Additionally, no debonding was identified using the conventional strain gauge instrumentation (Zorn 2006). The TR and SYM indices in Figure 11 and Figure 12 mostly remained below 0.2 except in sensing zone 7. As previously described, the outliers at sensing zone 7 are believed not to be related to debonding.

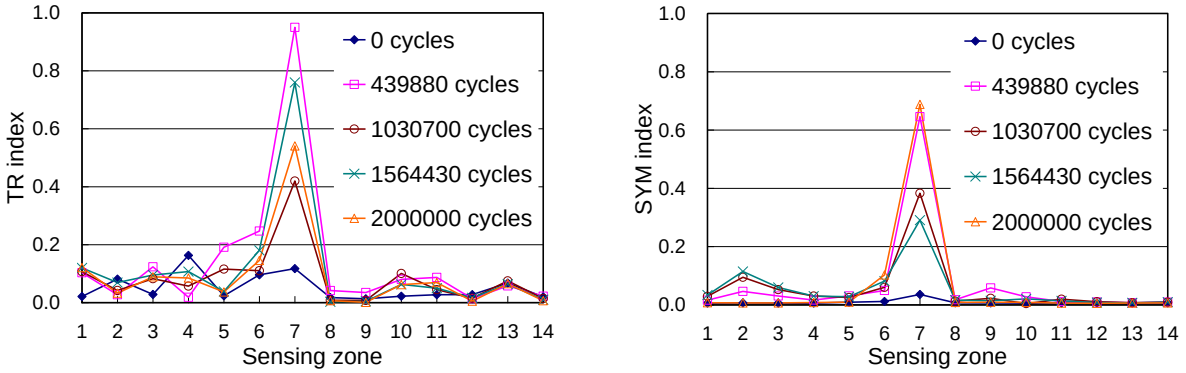

(a) TR indices at 5 selective numbers of fatigue cycles

(b) SYM indices at 5 selective numbers of fatigue cycles

Figure 11: Changes of the TR and SYM indices measured at selective numbers of cycles during the Case II fatigue loading test

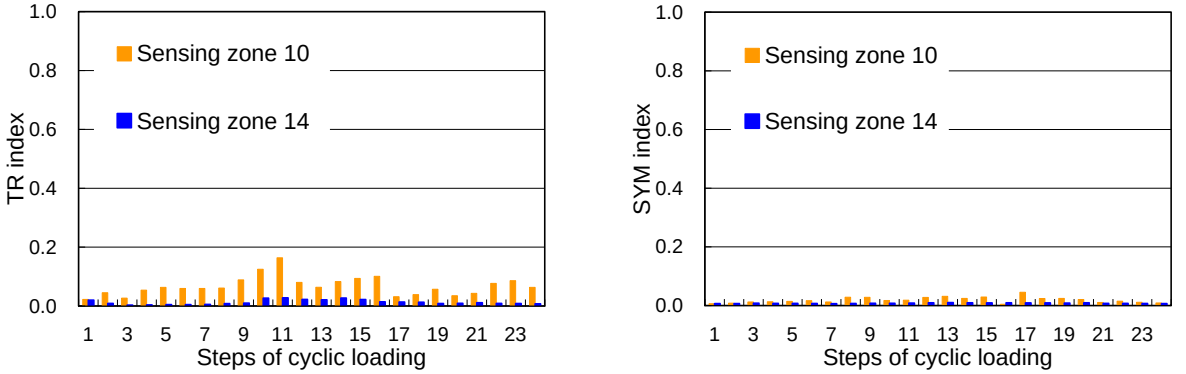

(a) TR indices at sensing zones 10 and 14

(b) SYM indices at sensing zones 10 and 14

Figure 12: Changes of the TR and SYM indices as a function of increasing fatigue load cycles measured at sensing zones 10 and 14 for Case II

5.3 Case III: Monotonic Loading Test after Fatigue Loading Test

After the Case II fatigue loading test, the same specimen was subjected to a monotonic loading test similar to that described in Section 5.1. As shown in Figure 13, the overall findings from Case III are similar to those described for Case I. The TR and SYM indices shown in Figure 14 further suggest that the debonding was initiated after loading step 11 near sensing zone 10. This finding is in agreement with that reported by Zorn (2006) based on conventional strain gauge data. However, the debonding became visible only after loading step 13 (see Figure 15(a)). This demonstrates that the proposed method may be able to provide an earlier warning of debonding than detailed visual inspection. Soon after the initial debonding was identified, the CFRP strip suddenly separated from the RC beam in a brittle manner. Figure 15(b) shows the fully detached CFRP layer after loading step 14. A closer examination of Figure 13 reveals that debonding initiated between PZT #9 and #10 and propagated toward PZT #15.

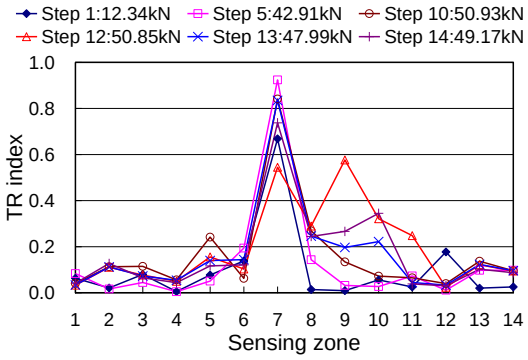

(a) TR indices at 6 loading steps

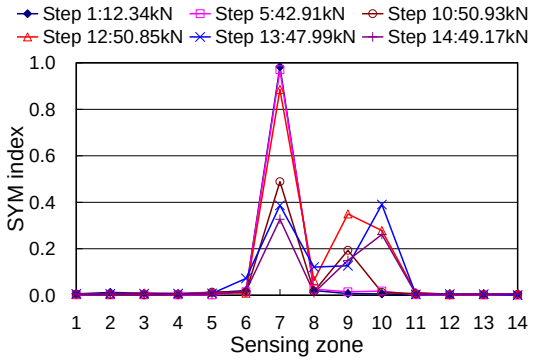

(b) SYM indices at 6 loading steps

Figure 13: Changes of the TR and SYM indices measured at selective loading steps during the Case III monotonic loading test

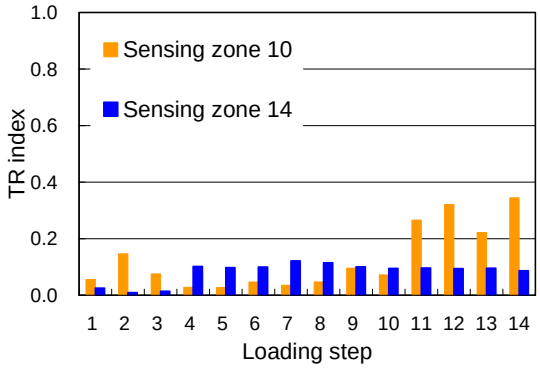

(a) TR indices at PZTs #10-#11 and #14-#15

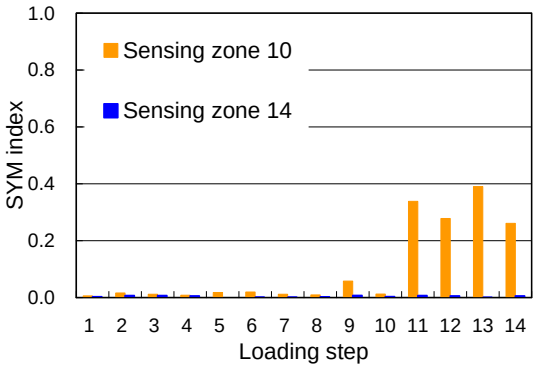

(b) SYM indices at PZTs #10-#11 and #14-#15

Figure 14: Change of the TR and SYM indices as a function of increasing monotonic loading measured at sensing zone 10 and 14 for Case III

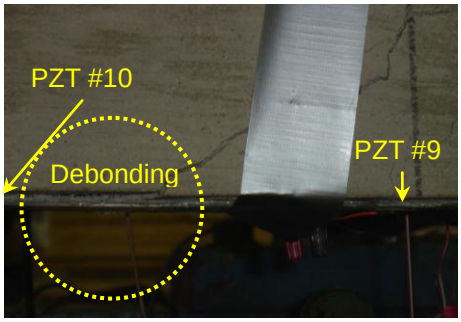

(a) Debonding identified between load steps 13 and 14

(b) Full debonding of the CFRP layer following load step 14

Figure 15: Visual inspection of debonding during the Case III monotonic test

6. CONCLUSION

In this study, a continuous monitoring system for detecting CFRP debonding from a host reinforced concrete structure is developed. The uniqueness of this study is in developing a new concept and theoretical framework of nondestructive testing (NDT), in which debonding is detected *without using previously obtained baseline data*. The potential of the proposed method is demonstrated using experimental data obtained from three loading tests of two CFRP strengthened RC beams: a monotonic load test (Case I), a fatigue load test (Case II), and a monotonic test following the fatigue load test (Case III). The proposed approach successfully estimated the initiation and region of debonding. The experimental results demonstrate the potential advantage of adopting the time reversal process for damage diagnosis over conventional approaches: It is expected that the proposed reference-free NDT technique is suitable for field deployment and is particularly effective in minimizing false-positive indications of defects. In addition, the proposed approach is able to sense over a larger area for debonding monitoring than conventional strain gauges or impedance measurements, which provide only discrete points or near-field measurements.

ACKNOWLEDGEMENT

The authors would like to thank Prof. Hoon Sohn at Carnegie Mellon University and Prof. Kent Harries at the University of Pittsburgh. The beam testing was conducted by Andrew Zorn and Benjamin Reeve in the Watkins-Haggart Structural Engineering Laboratory at the University of Pittsburgh.

REFERENCES

Akuthota, B., Hughes, D., Zoughi, R., Myers, J., and Nanni, A. (2004). "Near-Field Microwave Detection of Disbond in Carbon Fiber Reinforced Polymer Composites Used for Strengthening Cement-Based Structures and Disbond Repair Verification." *J. of Mater. in Civil Eng.*, 16(6), 540-546.

Ansari, F. (2005). "Fiber optic health monitoring of civil structures using long gage and acoustic sensors." *Smart Mater. and Struct.*, 14(3), S1-S7.

Draeger, C., Cassereau, D., and Fink, M. (1997). "Theory of the time-reversal process in solids." *J. Acoust. Soc. Am.*, 102(3), 1289-1295.

Ekenel, M., Stephen, V., Myers, J. J., and Zoughi, R. (2004). "Microwave NDE of RC Beams Strengthened with CFRP Laminates Containing Surface Defects and Tested Under Cyclic Loading." *Proc., 16th World Conference on Nondestructive Testing*, Montreal, Canada. August 30- September 3.

Feng, M. Q., Flaviis, F., and Kim, Y. J. (2000a). ''Use of Microwaves for Damage Detection of Fiber Reinforced Polymer-Wrapped Concrete Structure.'' *J. Eng. Mech.*, 128(2), 172–183.

Fink, M. (1999). "Time-Reversed Acoustics." *Scientific American*, 281(5), 91-97.

Fink, M., and Prada, C. (2001). "Acoustic Time-Reversal Mirrors." *Inverse Problems*, 17, R1-R38.

Giurgiutiu, V., Harries, K.A., Petrou, M.F., Bost, J., and Quattlebaum, J. (2003). "Disbond Detection with Piezoelectric Wafer Active Sensors in RC Structures Strengthened with FRP Composite Overlays." *Earthquake Eng. and Eng. Vibration*, 2(2), 213-224.

Giurgiutiu, V., and Lyshevski, S.E. (2004). *Micromechatronics: Modeling, analysis, and design with MATLAB*, CRC Press Inc, Boca Raton, FL.

Hong, S., and Harichandran, R. (2005). "Sensors to Monitor CFRP/Concrete Bond in Beams Using Electrochemical Impedance Spectroscopy." *J. of Composite for Construction*, 9(6), 515-523.

Ing, R.K., and Fink, M. (1996). "Time Recompression of Dispersive Lamb Waves using a Time Reversal Mirror – Application to Flaw Detection in Thin Plates." *Proc., 1996 IEEE Ultrasonics Symposium*, 1, 659-663.

Karbhari, V.M., Chin, J.W., and Reynaud, D. (2000). "Critical Gaps in Durability Data for FRP Composites in Civil Infrastructure." *Proc., 45th International Society for the Advancement of Materials and Process Engineering (SAMPE) Symposium and Exhibition*, Vol. 45, 549-563, Long Beach, CA, May 21-25.

Kessler, S. S., Johnson, C. E., and Dunn, C. T. (2003). "Experimental application of optimized Lamb wave actuating/sensing patches for health monitoring of composite structures." *Proc., of the 4th International Workshop on Structural Health Monitoring*, Stanford University, 429-436.

Levar, J. and Hamilton, H. (2003). "Nondestructive Evaluation of Carbon Fiber-Reinforced Polymer-Concrete Bond Using Infrared Thermography." *ACI Mater. J.*, 100(1), 63-72.

Luangvilai, K., Punurai, W., and Jacobs, L. (2002). "Guided Lamb Wave Propagation in Composite Plate/Concrete Component." *J. of Eng Mech.*, 128(12), 1337-1341.

Mal, A. K., Shih, F. J., Ricci, F., and Sauvik, B. (2005). "Impact damage detection in composite structures using Lamb waves." *Proc., of the SPIE*, 5768, 295-303.

Reeve, B. (2005). "Effect of Adhesive Stiffness and CFRP Geometry on the Behavior of Externally Bonded CFRP Retrofit Measures Subject to Monotonic Loads." MS Thesis, University of Pittsburgh Department of Civil and Environmental Engineering.

Rose, L. J. (1999). *Ultrasonic Waves in Solid Media*, Cambridge University Press, New York.

Sohn, H., (2006). "Effects of Environmental and Operational Variability on Structural Health Monitoring," *a Special Issue of Philosophical Transactions of the Royal Society on Structural Health Monitoring*, in press.

Sohn, H., Park, H., Law, K., and Farrar, C. (2006). "Combination of a Time Reversal Process and a Consecutive Outlier Analysis for Baseline-free Damage Diagnosis," *J. of Intelligent Mater. Systems and Structures*, in press.

Sun, F.P., Chaudhry Z., Liang, C., and Rogers C. A. (1995). "Truss Structure Integrity Identification Using PZT Sensor-Actuator." *J. of Intelligent Material Systems and Structures*, 6, 134-139.

Viktorov, I.A. (1967). *Rayleigh and Lamb Waves*, Plenum Press, New York.

Zorn, A. (2006). "Effect of Adhesive Stiffness and CFRP Geometry on the Behavior of Externally Bonded CFRP Retrofit Measures Subject to Fatigue Loads." MS Thesis, University of Pittsburgh Department of Civil and Environmental Engineering.